ACS Photonics

pubs.acs.org/journal/apchd5

Article

Broadband Nonvolatile Electrically Controlled Programmable Units in Silicon Photonics

Rui Chen, Zhuoran Fang, Johannes E. Fröch, Peipeng Xu, Jiajiu Zheng,* and Arka Majumdar*

Cite This: https://doi.org/10.1021/acsphotonics.2c00452

Read Online

ACCESS | Metrics & More | Article Recommendations | Supporting Information

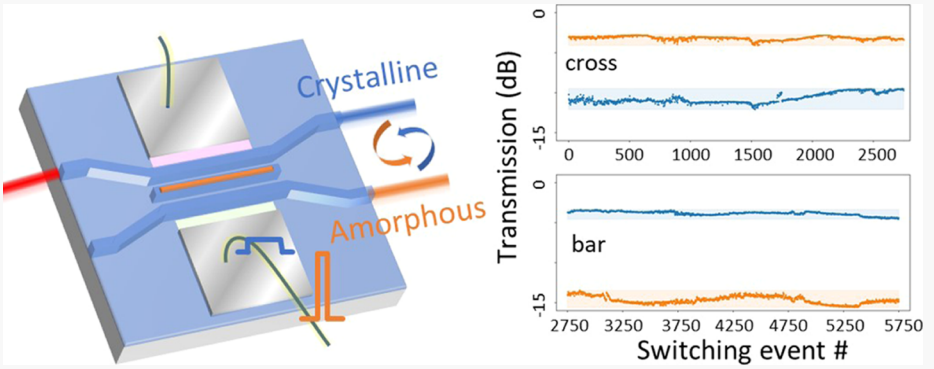

ABSTRACT: Programmable photonic integrated circuits (PICs) have recently gained significant interest because of their potential in creating next-generation technologies ranging from artificial neural networks and microwave photonics to quantum information processing. The fundamental building block of such programmable PICs is a **2 × 2 programmable unit**, traditionally controlled by the thermo-optic or free-carrier dispersion. However, these implementations are power-hungry and volatile and have a large footprint (typically >100 μm). Therefore, a truly "set-and-forget"-type **2 × 2 programmable unit** with zero static power consumption is highly desirable for large-scale PICs. Here, we report a broadband nonvolatile electrically controlled **2 × 2 programmable unit** in silicon photonics based on the phase-change material $Ge_2Sb_2Te_5$. The directional coupler-type programmable unit exhibits a compact coupling length (64 μm), small insertion loss (~2 dB), and minimal crosstalk (<−8 dB) across the entire telecommunication C-band while maintaining a record-high endurance of over 2800 switching cycles without significant performance degradation. This nonvolatile programmable unit constitutes a critical component for realizing future generic programmable silicon photonic systems.

KEYWORDS: *phase-change materials, reprogrammable photonics, zero static energy, silicon photonics*

INTRODUCTION

Photonic integrated circuits (PICs) typically have been application-specific,[1] that is, each fabricated chip serving only one particular function. In contrast, recent advancements in silicon photonics urgently call for universally programmable PICs,[2] adaptable to a wide range of tasks, including optical neural networks,[3] quantum information processing,[4] and light detection and ranging.[5] The fundamental building block constituting such programmable PICs is an electrically controlled 2 × 2 programmable unit or switch that diverts light to one of two ports. In silicon photonics, the operation of such elements is commonly based on either the thermo-optic[6] or free-carrier effect.[7] However, their functions are plagued by large footprints (typically >100 μm) and/or low energy efficiency because of large static power consumption. Although ring resonators can significantly reduce the footprint (down to the order of tens of μm), the operational optical bandwidth becomes limited to typically less than 1 nm.[8] Moreover, their thermal instability requires an even larger static power consumption, as a constant feedback signal is needed to lock the resonance.[9] Emerging technologies such as micro-electromechanical systems (MEMS),[10] electro-optic polymer,[11] and integrated lithium niobate[12] can potentially provide either a smaller footprint or lower programming energy. Still, they are all based on volatile effects with limited complementary metal-oxide-semiconductor (CMOS) compatibility. Phase-change materials (PCMs) provide an attractive solution toward compact and energy-efficient programmable units with zero static power,[13−16] thanks to a nonvolatile phase transition,[17] large refractive index contrast ($\Delta n \geq 1$),[18] and CMOS compatibility.[15]

Received: March 22, 2022

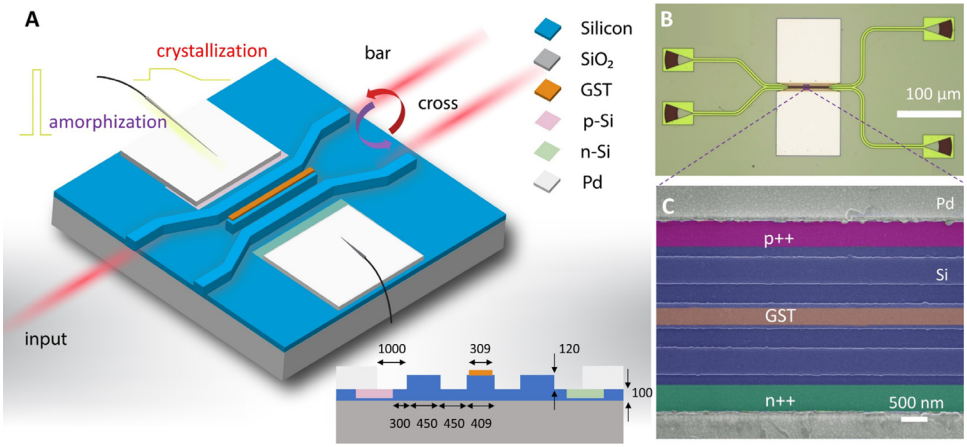

Figure 1. Broadband nonvolatile electrically controlled 2 × 2 programmable unit in silicon photonics. (a) Device schematic. Inset: The cross-sectional view at the center of the device. The 40 nm encapsulation Al_2O_3 is not shown. (b) The optical micrograph and (c) SEM images of the device. In the SEM image, the GST thin film, p++, and n++ regions are indicated by false colors.

Pulsed laser-induced switching of PCMs for all-optical applications, such as optical memories[19−23] and optical computing,[24−27] has been studied extensively. However, this approach usually involves complex optical alignment, which precludes simultaneous multidevice control and is generally unsuitable for large-scale applications. Recently, the phase transition has been actuated on-chip electrically via doped silicon[28−33] and/or ITO heaters,[34−36] achieving reversible tuning and a large cyclability of ∼500 cycles.[28] However, thus far, no broadband electrically controlled 2 × 2 programmable unit based on $Ge_2Sb_2Te_5$ (GST) has been demonstrated. While such functionality is ultimately indispensable for large-scale reprogrammable photonic applications, the inherent high absorptive loss of crystalline GST (c-GST)[37] becomes a severe issue for most designs (see the Supporting Information, Section S2.1). Existing electrically tunable GST devices are either designed only for 1 × 1 switches[28,35] or rely on ring resonators[28,38] to circumvent the loss issue. The former is clearly not suitable for encoding information in different optical paths, or spatial information encoding. Thus, it has limited applications in programmable photonics for applications such as optical switch fabric and information processing.[2,3,6,39] While the latter is suitable for spatial information encoding in a narrow band, a broadband design is preferred to access a wider optical wavelength range.

We report a broadband nonvolatile electrically controlled 2 × 2 programmable unit in silicon photonic based on the technologically mature PCM GST. The directional coupler-based photonic unit features a compact footprint of only 64 μm coupling length. The measured insertion loss and crosstalk are less than 2 and −8 dB in both bar and cross states across the entire telecommunication C-band, respectively. We experimentally demonstrate a record-high endurance for operation over 2800 switching cycles, that is, over 5600 switching events. The fabrication of the programmable unit is fully compatible with standard CMOS foundry processes, promising excellent scalability. Therefore, our work represents a crucial step toward realizing compact and energy-efficient programmable silicon PICs.

RESULTS

Device Design and Fabrication. Our electrically controlled 2 × 2 programmable unit leverages an asymmetrical three-waveguide directional coupler structure[13,40,41] fabricated in a silicon on insulator (SOI) platform combined with an on-chip P-I-N (p++-doped-intrinsic-n++-doped) heater, as shown in Figure 1a. Compared to previous studies, where rapid thermal annealing[13,42] was used to change the PCM phase, our devices can be reliably and reversibly switched with short electrical pulses via on-chip PIN micro-heaters for more than 2800 cycles. The design consists of two Si transmission waveguides with a coupling region separated by a truncated transition waveguide. To circumvent the high absorption loss of c-GST, only the transition waveguide is loaded with a 20 nm thick GST, encapsulated by 40 nm Al_2O_3 to prevent GST oxidation. By design, the phase-matching condition is satisfied only when the GST is switched to the amorphous state (a-GST), which allows light to couple into the transition waveguide and further to the cross port. However, if the GST is in the crystalline state, light barely couples into the transition waveguide because of a significant index mismatch, thus bypassing the high loss of c-GST. The gap between the waveguides is designed to achieve a good tradeoff between insertion loss and device footprint. Our simulations show an insertion loss of less than 1 dB, extinction ratio of larger than 13 dB at 1520 nm, and a 1 dB bandwidth larger than 50 nm (Supporting Information, Section S2). While similar designs have been reported before,[13,40] it is noteworthy that electrical tunability was not demonstrated in such programmable unit designs, primarily due to the lack of suitable heater designs for large-volume GST switching. A PIN heating element implements the electrical control over phase switching, which is realized by selectively doping the adjacent regions to the waveguide. We note that this concept directly extends our prior studies, where we implemented this concept[28] for a 1 × 1 switch. However, in contrast to the previous 1 × 1 programmable unit work, this work demonstrates a 2 × 2 programmable unit, which can be used in a lot more applications, thanks to its suitability for spatial information encoding. Moreover, the volume of the GST being electrically switched experimentally is ∼0.4 μm^3 in the present work, around ten times larger.[28,34−36] Therefore, prior to fabrication, we optimized the design and operation of the PIN microheater and device transmission using finite element simulations,[28,43] considering the device's electrical and heat transfer transient performance (Supporting Information, Section S3). We also

https://doi.org/10.1021/acsphotonics.2c00452
ACS Photonics XXXX, XXX, XXX−XXX

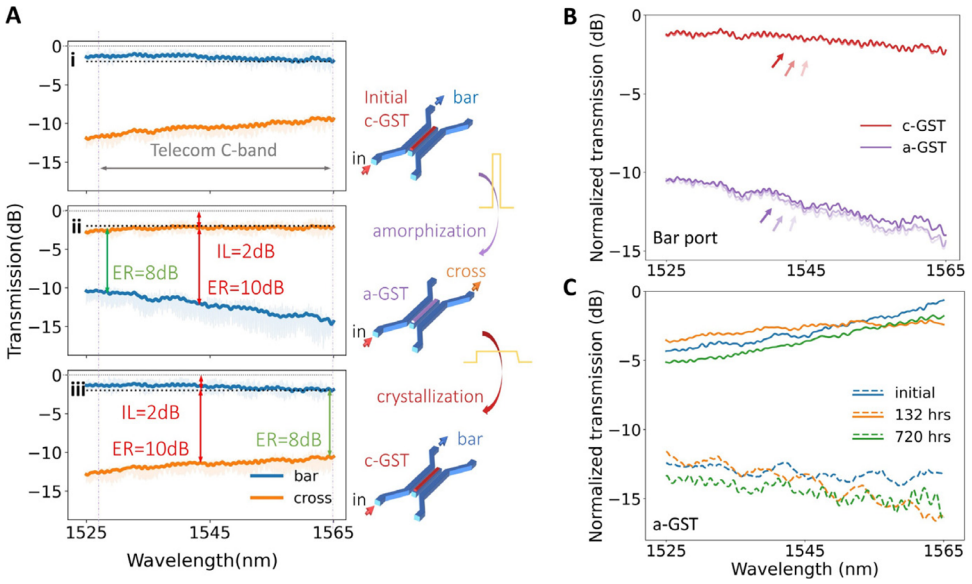

Figure 2. Characterizations of the electrically controlled 2 × 2 programmable unit. (a) Transmission spectrum of the device (i) initially, (ii) after applying an amorphization pulse, and (iii) after applying a crystallization pulse. The shaded areas are the measured raw spectra, and the solid lines are spectra after a low pass filter. IL and ER are insertion loss and extinction ratio, respectively. (b) Transmission spectra measured over three cycles at the bar port. Each cycle is indicated with different color saturations. (c) Device functionality over an extended period of one month with a-GST. The solid and dashed lines correspond to the bar and cross port transmission.

stress that compared with resistor-type heaters such as metal, P-I-P, or N-I-N heaters, PIN heaters are more energy-efficient. This can be intuitively understood by recognizing the electric current in the PIN diode, which increases exponentially with voltage (see the Supporting Information, Section S4.1, Figure S11c), while that of resistor-type heaters only grows linearly.

The fabricated device's optical and scanning electron microscopy (SEM) images are shown in Figure 1b,c, respectively. In detail, the PCM phase is switched by an on-chip P-I-N heater, defined by doping the 100 nm thick silicon slab via ion implantation while leaving the three waveguides intrinsic[28] to reduce the insertion loss (see Methods for fabrication details). The doped regions and metal pads are designed to maintain a distance of 200 nm and 1 μm, respectively, from the directional coupler to reduce excess loss from the free carriers.

Reversible Switching Characterization. The reversible operation of the electrically controlled 2 × 2 programmable unit is demonstrated by measuring the transmission of a tunable laser through the bar and cross port at two different phases of GST, as summarized in Figure 2a. Initially, the GST is prepared in the crystalline state (c-GST), for which the light passes through the bar port with an extinction ratio over 10 dB at 1550 nm and over 8 dB across the entire C-band (Figure 2a(i)). After applying a short, high amplitude pulse (13.6 V, 8 ns leading/falling edge, 200 ns pulse width with 380 nJ pulse energy) to induce amorphization (a-GST), the transmission spectrum flips, resulting in a high transmission through the cross port with over 10 dB extinction ratio at 1550 nm and over 8 dB across the entire C-band (Figure 2a(ii)). Subsequently, we applied a longer but lower amplitude pulse (3.2 V, 8 ns leading edge, 50 μs pulse width with 6.83 μJ pulse energy) to trigger crystallization, returning the switch to the original high bar transmission state (Figure 2a(iii)). Crosstalk less than −8 dB is observed across the entire telecommunication C-band (1530 to 1565 nm) in cross and bar states. We estimate the switching energy density to be 0.95/1.63 fJ/nm^3 for amorphization/crystallization. This is comparable with a previous study result,[28] where an energy density of 0.2/1.95 fJ/nm^3 for the phase transition was demonstrated. The cycle-to-cycle reproducibility was verified over three consecutive switching cycles, as shown in Figure 2b, where transmission spectra for a-GST and c-GST at the bar port overlap nearly perfectly. We then established the long-term retention of the device states by performing several measurements over a period of one month, as shown in Figure 2c. A good match between the transmission spectra for devices in the a-GST configuration after putting the device in an ambient environment for 132 and 720 h indicates that the switching is indeed nonvolatile. Slight variations among the spectra are likely due to minor differences in the optical alignment during the different measurements.

Cyclability Test Results. Finally, we demonstrate reversible operation over 5750 switching events measured at 1550 nm without significant performance degradation, as presented in Figure 3 (additional measurement results are shown in the Supporting Information, Section S4.1), thanks to the optimized PIN heater design. We note that because of limitations in our measurement setup (see Methods for measurement details), the cross and bar ports are measured consecutively, as shown in Figure 3(top) and (bottom), respectively. The two distinct transmission levels arising from switching between the crystalline and amorphous states are indicated by the shaded regions, whereas transmission contrasts of 8 and 11 dB are obtained for the cross and bar ports, respectively. The measured insertion loss at the beginning is around 1 dB higher compared to that shown Figure 2, which can be attributed to the fiber alignment variation as well as device performance degradation due to previous measurement steps. Interestingly, although the cross-port transmission contrast reduces from 8 to 6 dB at the 2750th event, the bar port contrast remains around 11 dB throughout the measurement. We attribute this reduction in the cross-port transmission contrast to thermal reflowing and

https://doi.org/10.1021/acsphotonics.2c00452
ACS Photonics XXXX, XXX, XXX−XXX

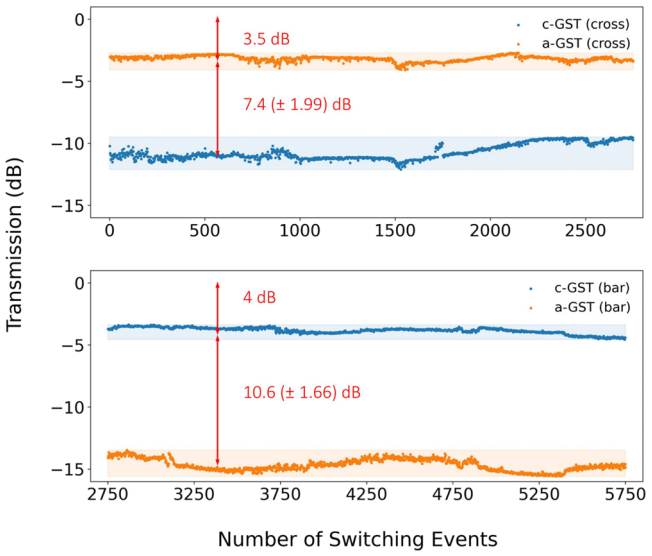

Figure 3. Cyclability test of the electrically controlled 2 × 2 programmable unit. (Top) Transmission measured at the cross port. (Bottom) Transmission measured at the bar port. Blue/orange dots represent the measured transmission at 1550 nm after sending in a crystallization/amorphization pulse (with the same pulse condition in Figure 2). The shaded regions correspond to the variations of the two distinct transmission levels. A larger insertion loss of 3 dB at both ports at the beginning can be attributed to fiber alignment variation as well as the material degradation and thermal reflowing of the GST thin film in previous measurement steps, see the Discussion section.

material degradation of GST after multiple cycles (Supporting Information, Section S7). The performance degradation is less pronounced for the bar port because even if the GST shape changes due to thermal reflowing, a significant index mismatch still exists between the transition waveguide and input waveguide (see the Supporting Information, Figure S7e) so that light still does not couple to the transition waveguide. We note that some data points are removed around the 600th, 800th, and 1900th events because the same amorphization condition failed to trigger phase change, and larger voltages of 13.8, 14.1, and 14.4 V were used after that, respectively. This could result from drifting contacts of electrical probes (Supplementary Section S4, Figure S10c) and/or GST degradation. The contact drift issue could be solved by wire-bonding the chip to a carrier.

One-by-One and One-by-Two Programmable Unit Results. In addition to the electrically controlled 2 × 2 programmable unit, we also demonstrated an electrically controlled 1 × 2 programmable unit and a waveguide-based 1 × 1 switch on the GST-on-SOI platform (Supplementary Materials). The 1 × 2 programmable unit consists of two mutually coupled waveguides, one of which is loaded with 20 nm GST thin film. The two waveguides are designed in a similar fashion as in the 2 × 2 programmable unit that the phase-matching condition is satisfied when GST is in the amorphous state, while a large mismatch happens when it is switched into the crystalline state. Light from the bare silicon waveguide can then efficiently couple into the GST-loaded waveguide for a-GST but remains in the bar waveguide for c-GST. This programmable unit shows an extinction ratio of 9 dB over 15 nm wavelength range in both amorphous and crystalline states and an excellent endurance of more than 4000 cycles (Supporting Information, Section S4.2). The waveguide-based 1 × 1 switch is a 10 μm long waveguide loaded with 20 nm thick GST thin film. The programmable unit exhibits a large extinction ratio of more than 10 dB, the capability of multilevel switching with ten distinct transmission levels, and excellent endurance of more than 1000 switching cycles (Supporting Information, Section S4.3). We observed that the extinction ratio increases from 10 dB to around 20 dB after initial cycles (see the Supporting Information, Section S4.3), which is a well-known PCM conditioning phenomenon.[20,44] Potential applications of these electrically controlled programmable units are discussed in Supplementary Section S7, where nonvolatile PICs for energy-efficient optical routing, OPGA, and optical computing are proposed.

Table 1. 1 × 2 or 2 × 2 Programmable Unit Performance Comparison[a,b]

ref	structure	mechanism	ER (dB)	IL (dB)	energy per second (nJ/s)	footprint in length (μm)	optical BW (nm)	nonvolatile	tuning method and cycles
53	MZI	thermal	>20.0	0.5	1.3×10^7	>200	>70	no	electrical
7	MZI	free carrier	4.5	10.0	2.7×10^9	1.3×10^4	N. R.	no	electrical
12	MZI	EO LN	40.0	2.5	1.9×10^7	5.0×10^4	>40	no	electrical
54	MZI	EO polymer	>25.0	8.2	8.5×10^6	1.5×10^4	N. R.	no	electrical
8	MDR	thermal	7.0	0.8 /9.0[c]	1.5×10^7	12.8	< 0.5	no	electrical
55	MRR	free carrier	>20.0	~0	9.7×10^6	35	<0.1	no	electrical
56	MRR	MEMS	>20.0	2.0/0.1[c]	600	4	<2	no	electrical
46	MRR	PCM	>5.0	5.1/4.3[c]	0.19 (17.1)[e]	60	<1	yes	optical, 1000 cycles
38	MRR	PCM	14	0.75/ 0.46[c]	0.25 (11)[e]	25	<1	yes	optical
13	DC	PCM	>10	1.0	N. R.	45	>30	yes	RTA
45	MMI	PCM	8.0	0.5	14 (9.5×10^5)[e]	43	N. R.	yes	optical
30	MZI	PCM	6.5 (cross)/15.0 (bar)	>0.3	176 (3.8×10^3)[e]	>100[d]	>15[d]	yes	electric, >125 cycles
this work	DC	PCM	10.0	2.0	380 (6.8×10^3)[e]	50	>30	yes	electric, >2800 cycles

[a]ER: extinction ratio, IL: insertion loss, BW: bandwidth, MZI: Mach−Zehnder Interferometer, MR(*D*)R: micro-ring(disk) resonator, DC: directional coupler, EO: electro-optic effect, LN: $LiNbO_3$, N.R.: not reported. [b]Note: For devices based on nonvolatile effects, energy consumption is estimated as the energy per switching event, assuming one second per switching event. [c]For drop and through ports, respectively. [d]Estimated from figures. [e]Energy per switching event for amorphization (crystallization).

https://doi.org/10.1021/acsphotonics.2c00452
ACS Photonics XXXX, XXX, XXX−XXX

DISCUSSION

Table 1 compares our device to other reported 2 × 2 programmable units over different performance metrics. For devices based on a volatile effect, the energy consumption equals the energy per second. For those based on nonvolatile effects, the energy consumption is defined as the energy per switching event. This comparison is reasonable because programmable PICs, such as for optical information processing,[3,24,27] usually work in the low electrical frequency, that is the switching events are not happening constantly in a short period. Hence, volatile switches impose a constant drain in the energy over one second, while the nonvolatile ones do not consume energy after the initial switching event. From Table 1, our 2 × 2 programmable unit shows several orders of magnitude reduction in the device footprint and energy consumption compared to the volatile schemes except for the MEMS, which is inherently challenging to fabricate. Our work also compares favorably to previously reported PCM-based photonic switches[13,28,38,45,46] in terms of the largest reported bandwidth (>30 nm), electrical tunability, large extinction ratio in both cross and bar states (>10 dB at 1550 nm and >8 dB across the entire C-band), and the highest reported endurance (>2800 cycles) in PCM-based devices.

We further demonstrate the thermal stability advantage of our broadband 2 × 2 programmable unit over the narrowband designs using a thermal stability test. It is well known that thermal feedback control is required for the stable operation of microring resonators because of their sensitivity to thermal fluctuation.[9] We performed a thermal stability test on our broadband 2 × 2 programmable unit (Supplementary, Section S5) by varying the temperature from 25 to 35 °C, and no significant spectrum drift was observed. Such invariant to thermal fluctuations renders our switches even more energy efficient as no extra energy is needed for temperature control.

The transient response of our nonvolatile programmable unit is shown in Supplementary Section S6. The amorphization response time is much longer than the electrical pulse duration (200 ns) and is estimated at around 1(2.5) μs at the bar(cross) port. We attribute this to the slow minority carrier injection process when the PIN diode is forward biased with a large voltage. On the other hand, because of a much smaller peak voltage, the crystallization response time is almost the same as the total pulse duration of 80 μs. This crystallization time can be reduced to hundreds of nanoseconds by further exploring the crystallization condition.[21] We stress again that the response speed is not a crucial figure of merit considering the application areas of our device. The main advantage of our programmable unit is its nonvolatile nature. Such a device consumes zero static energy and thus can be used as a fundamental building block for reprogrammable photonics, generally low-speed applications. This is quite different from a modulator scenario, where high speed is essential. For example, let us consider how the field-programmable gate array (FPGA) works. The desired function can be implemented by reconfiguring the programmable units (configurable logic blocks). Depending on the users' needs, this function may be held for hours, days, or even months. In this case, whether the programmable unit can be configured in ten microseconds or ten nanoseconds does not make a significant difference to the system performance because the overhead is already minimal. However, the energy saved is enormous during the static operation compared with thermo-optic, carrier dispersion, or electro-optic effect-based devices, as discussed in previous parts.

The relatively high insertion loss of our 2 × 2 programmable unit in the experiment (~2 dB at 1550 nm) compared to the simulation (<1 dB, see Supplementary Section S2.3) can be attributed to several factors. First, fabrication imperfections such as variations in etch depth and waveguide, and GST width (Supplementary, Section S7, Figure S17) could all lead to an increase in device insertion loss (Supplementary, Section S2.4). Hence, we believe that the insertion loss can be reduced to <1 dB based on our simulations with optimized fabrication conditions. Second, a tradeoff between the insertion loss in the two states can be observed in Figures S4 and S5 (Supplementary, Section S2) because of the finite loss of amorphous GST. This can be resolved by replacing GST with recently reported low-loss PCMs such as Sb_2S_3 and Sb_2Se_3.[47−50] However, we note that the choice of GST is preferred for compatibility with existing high-volume manufacturing because this material has been extensively studied in electronic memories and is technologically mature.[17,51]

Although our 2 × 2 programmable unit displayed the highest reported cyclability among electrically controlled PCM-based photonic devices (we note a work came out during the review of this study shows half million cycles operations using a tungsten heater[52]), it is still significantly lower than the records obtained for electronic memories (~10^{12} cycles, potentially scale up to 10^{15}cycles).[17,51] The cyclability of our device is mainly limited by thermal reflowing and material ablation because of the large GST volume (Supplementary, Section S7). To improve the cyclability further, instead of using a long (64 μm) GST thin film, one can leverage the subwavelength grating structure, where periodic GST nanodisks or nanostrips with a much smaller length (down to 100 nm) can significantly reduce the volume of each GST cell, thus easing the thermal reflow issue.[27,38] The choice of encapsulation material turns out to be crucial to achieve better device endurance. In our experiment, encapsulation with atomic layer deposition Al_2O_3 showed the best performance because of the highly conformal and plasma-free nature. A thicker Al_2O_3 capping layer could also be used to further avoid material oxidation and thermal reflowing, for example, a 218 nm Al_2O_3 capping layer is used in a previous study.[27]

CONCLUSIONS

In summary, we have demonstrated a broadband nonvolatile electrically controlled 2 × 2 programmable unit. Driven by an on-chip PIN microheater, the 2 × 2 programmable unit can be reversibly and reliably switched for more than 2800 cycles without significant performance degradation. The cross and bar states maintain small cross-talk (<−8 dB) and insertion loss (~2 dB) across the entire telecommunication C-band in the experiment. The 2 × 2 programmable unit is compatible with CMOS manufacturing processes and has a compact footprint of 64 μm coupling length. The insertion loss of the device can be further reduced by more optimized fabrication and by replacing GST with low-loss PCMs.[47−50] This work constitutes a crucial element for realizing zero static consumption and compact universal programmable PICs for on-chip nonvolatile light routers, optical programmable gate arrays, neuromorphic computing, and quantum information processing.

https://doi.org/10.1021/acsphotonics.2c00452
ACS Photonics XXXX, XXX, XXX−XXX

METHODS

SOI Device Fabrication. Our electrically controlled 2 × 2 programmable units were fabricated on a commercial SOI wafer with 220 nm thick silicon on 3 μm thick SiO_2 (SOITECH). The rib waveguides and grating couplers were defined with electron-beam lithography (EBL, JEOL JBX-6300FS) using a positive tone E-beam resist (200 nm thick ZEP-520A) and partially etched by 120 nm in a fluorine-based inductively coupled plasma etcher (ICP, Oxford PlasmaLab 100 ICP-18) using a mixed gas of SF_6 and C_4F_8. The etching rate was calibrated each time before the etching to ensure a correct etch depth. The doping regions were defined by two additional EBL steps with 600 nm thick poly (methyl methacrylate) (PMMA) resist and implanted by boron (phosphorus) ions for p++(n++) with a dosage of 2×10^{15} ions per cm^2 and an ion energy of 14 keV (40 keV). A tilt angle of 7° while conducting ion implantation was used to misalign with the silicon lattice and thus achieve uniform deep doping. To activate the dopants, the chips were annealed at 950 °C for 10 min (Expertech CRT200 Anneal Furnace). Before metal contact deposition, to ensure an ideal Ohmic contact, the surface native oxide was removed by immersing the chips in a 10:1 buffered oxide etchant (BOE) for 10 s. The metal contacts were then immediately patterned by a fourth EBL step using PMMA and formed by electron-beam evaporation (CHA SEC-600) and lift-off of Ti/Pd (5 nm/180 nm) layers. After a fifth EBL defining the GST window, a 20 nm GST thin film was deposited using a GST target (AJA International) in a magnetron sputtering system (Lesker Lab 18), followed by a lift-off process. The deposition rate was calibrated on a silicon chip using an ellipsometer (Woollam alpha-SE). The GST is then encapsulated by 40 nm thick Al_2O_3 through ALD (Oxford Plasmalab 80PLUS OpAL ALD) at 150 °C. To ensure good contact between the electric probe and metal pads while measuring, Al_2O_3 on the metal contacts was removed by defining a window using a sixth EBL with 600 nm PMMA and then etching in a chlorine-based inductively coupled plasma etcher (ICP-RIE, Oxford PlasmaLab 100 ICP-18). Finally, rapid thermal annealing (RTA) at 200 °C for 10 min was conducted to completely crystallize the GST.

Optical Simulation. The refractive index data for GST were measured and fitted using an ellipsometer (Woollam M-2000).[13] The nonvolatile switches were designed (verified) by a commercial photonic simulation software package Lumerical MODE(FDTD). See Supplementary Material, Section S2.

Heat-Transfer Simulation. The heat-transfer performance of the silicon PIN microheater was simulated with a commercial Multiphysics simulation software COMSOL Multiphysics.[28,43] In the simulation, a heat-transfer model is coupled with a semiconductor model to simulate the transient time performance of the microheater and to determine the phase-change conditions. See Supplementary Materials, Section S3.

Steady-State Optical Measurement Setup. The programmable units were measured with a vertical fiber-coupling setup using a coupling angle of 25° (Supplementary Section S1). The stage temperature was fixed at 26 °C controlled using a thermoelectric controller (TEC, TE Technology TC-720). A tunable continuous-wave laser (Santec TSL-510) provided the input light. The polarization was controlled using a manual fiber polarization controller (Thorlabs FPC526) to match the TE mode of the rib waveguides. A low-noise power meter (Keysight 81634B) was used to measure the static optical transmission from the output grating couplers. The transmission spectra of the devices were obtained by normalizing to the closest reference waveguide spectra. For the $I-V$ characterization and on-chip electrical switching, electrical pulses were applied to the on-chip metal contacts via a pair of electrical probes controlled by two probe positioners (Cascade Microtech DPP105-M-AI-S). In particular, the $I-V$ curve measurement was performed using a source meter (Keithley 2450), which is later used to estimate the power of the applied pulses. The crystallization and amorphization pulses were generated from a pulse function arbitrary generator (Keysight 81160A). The tunable laser, power meter, thermal controller, source meter, and pulse function arbitrary generator are controlled using a laptop with a National Instrument interface.

Transient Response Measurement Setup. The transient response of the programmable units was measured under the same vertical fiber coupling setup. Instead of the power meter, we used a switchable gain balanced amp photodetector (Thorlabs, PDB450C) with 150 MHz bandwidth to obtain the fast time response. An optical amplifier (Amonics AEDFA-30-B-FA) was used to amplify the optical signal to ∼1 mW before the photodetector so that the photodetector operates in its linear range. The photodetector response was captured using an oscilloscope, triggered by the applied electrical signal. (See Supplementary Materials, Section S1).

ASSOCIATED CONTENT

Supporting Information

The Supporting Information is available free of charge at https://pubs.acs.org/doi/10.1021/acsphotonics.2c00452.

Figure S1: measurement setup; Figure S2: complex refractive indices of a/c-GST; Figure S3: schematic of the 1 × 2 programmable unit; Figure S4: mode simulation of the 1 × 2 programmable unit; Figure S5: mode simulation of the 2 × 2 programmable unit; Figure S6: FDTD simulation of both 1 × 2 and 2 × 2 programmable units; Figure S7: insertion loss vs fabrication variation simulation study; Figure S8: extinction ratio vs fabrication variation simulation study; Figure S9: transient heat-transfer simulation; Figure S10: full endurance test results; Figure S11: additional measurement results; Figure S12: transmission measurement results for the 1 × 2 programmable unit; Figure S13: endurance test results for the 1 × 2 programmable unit; Figure S14: measurement results for the waveguide switch; Figure S15: thermal stability test; Figure S16: transient response measurement results; Figure S17: SEM of the devices; Figure S18: applications envision (PDF)

AUTHOR INFORMATION

Corresponding Authors

Jiajiu Zheng − *Department of Electrical and Computer Engineering, University of Washington, Seattle, Washington 98195, United States;* orcid.org/0000-0003-1527-201X; Email: jjzno1@gmail.com

Arka Majumdar − *Department of Electrical and Computer Engineering and Department of Physics, University of Washington, Seattle, Washington 98195, United States;* orcid.org/0000-0003-0917-590X; Email: arka@uw.edu

https://doi.org/10.1021/acsphotonics.2c00452
ACS Photonics XXXX, XXX, XXX−XXX

Authors

Rui Chen − *Department of Electrical and Computer Engineering, University of Washington, Seattle, Washington 98195, United States;* orcid.org/0000-0001-8492-729X

Zhuoran Fang − *Department of Electrical and Computer Engineering, University of Washington, Seattle, Washington 98195, United States;* orcid.org/0000-0001-8724-6633

Johannes E. Fröch − *Department of Electrical and Computer Engineering, University of Washington, Seattle, Washington 98195, United States*

Peipeng Xu − *Faculty of Electrical Engineering and Computer Science, Key Laboratory of Photoelectric Materials and Devices of Zhejiang Province, Ningbo University, Ningbo 315211, China*

Complete contact information is available at: https://pubs.acs.org/10.1021/acsphotonics.2c00452

Author Contributions

J.Z. and A.M. conceived the project. R.C. simulated the nonvolatile switches, fabricated the samples, and performed optical characterizations and data analysis. J.Z. optimized and simulated all the devices, planned the layout, and helped with data analysis. Z.F. fabricated and measured test structures, and helped with other fabrications, optical measurements, and data analysis. J.F. helped with device characterization. P.X. helped with the FDTD simulation and discussed with J.Z. about the design. A.M. supervised and planned the project. R.C. wrote the manuscript with inputs from all the authors.

Funding

The research is funded by the National Science Foundation (NSF-1640986, NSF-2003509), ONR-YIP Award, DARPA-YFA Award, DRAPER Labs and Intel.

Notes

The authors declare no competing financial interest.

■ ACKNOWLEDGMENTS

We thank Prof. Sajjad Moazeni at the University of Washington for letting us use his high-speed photodetector to characterize the transient response. Part of this work was conducted at the Washington Nanofabrication Facility/Molecular Analysis Facility, a National Nanotechnology Coordinated Infrastructure (NNCI) site at the University of Washington, which is supported in part by funds from the National Science Foundation (awards NNCI-1542101, 1337840, and 0335765), the National Institutes of Health, the Molecular Engineering & Sciences Institute, the Clean Energy Institute, the Washington Research Foundation, the M. J. Murdock Charitable Trust, Altatech, ClassOne Technology, GCE Market, Google, and SPTS.

■ REFERENCES

(1) Chen, X.; Milosevic, M. M.; Stanković, S.; Reynolds, S.; Bucio, T. D.; Li, K.; Thomson, D. J.; Gardes, F.; Reed, G. T. The Emergence of Silicon Photonics as a Flexible Technology Platform. *Proc. IEEE* **2018**, *106*, 2101−2116.

(2) Bogaerts, W.; Pérez, D.; Capmany, J.; Miller, D. A. B.; Poon, J.; Englund, D.; Morichetti, F.; Melloni, A. Programmable Photonic Circuits. *Nature* **2020**, *586*, 207−216.

(3) Shen, Y.; Harris, N. C.; Skirlo, S.; Prabhu, M.; Baehr-Jones, T.; Hochberg, M.; Sun, X.; Zhao, S.; Larochelle, H.; Englund, D.; Soljačić, M. Deep Learning with Coherent Nanophotonic Circuits. *Nat. Photonics* **2017**, *11*, 441−446.

(4) Arrazola, J. M.; Bergholm, V.; Brádler, K.; Bromley, T. R.; Collins, M. J.; Dhand, I.; Fumagalli, A.; Gerrits, T.; Goussev, A.; Helt, L. G.; Hundal, J.; Isacsson, T.; Israel, R. B.; Izaac, J.; Jahangiri, S.; Janik, R.; Killoran, N.; Kumar, S. P.; Lavoie, J.; Lita, A. E.; Mahler, D. H.; Menotti, M.; Morrison, B.; Nam, S. W.; Neuhaus, L.; Qi, H. Y.; Quesada, N.; Repingon, A.; Sabapathy, K. K.; Schuld, M.; Su, D.; Swinarton, J.; Száva, A.; Tan, K.; Tan, P.; Vaidya, V. D.; Vernon, Z.; Zabaneh, Z.; Zhang, Y. Quantum Circuits with Many Photons on a Programmable Nanophotonic Chip. *Nature* **2021**, *591*, 54−60.

(5) Rogers, C.; Piggott, A. Y.; Thomson, D. J.; Wiser, R. F.; Opris, I. E.; Fortune, S. A.; Compston, A. J.; Gondarenko, A.; Meng, F.; Chen, X.; Reed, G. T.; Nicolaescu, R. A Universal 3D Imaging Sensor on a Silicon Photonics Platform. *Nature* **2021**, *590*, 256−261.

(6) Pérez, D.; Gasulla, I.; Crudgington, L.; Thomson, D. J.; Khokhar, A. Z.; Li, K.; Cao, W.; Mashanovich, G. Z.; Capmany, J. Multipurpose Silicon Photonics Signal Processor Core. *Nat. Commun.* **2017**, *8*, 636.

(7) Liao, L.; Samara-Rubio, D.; Morse, M.; Liu, A.; Hodge, D.; Rubin, D.; Keil, U. D.; Franck, T. High Speed Silicon Mach-Zehnder Modulator. *Opt. Express* **2005**, *13*, 3129−3135.

(8) Zhang, W.; Yao, J. Photonic Integrated Field-Programmable Disk Array Signal Processor. *Nat. Commun.* **2020**, *11*, 406.

(9) Atabaki, A. H.; Moazeni, S.; Pavanello, F.; Gevorgyan, H.; Notaros, J.; Alloatti, L.; Wade, M. T.; Sun, C.; Kruger, S. A.; Meng, H.; Al Qubaisi, K.; Wang, I.; Zhang, B.; Khilo, A.; Baiocco, C. V.; Popović, M. A.; Stojanović, V. M.; Ram, R. J. Integrating Photonics with Silicon Nanoelectronics for the next Generation of Systems on a Chip. *Nature* **2018**, *556*, 349−354.

(10) Errando-Herranz, C.; Takabayashi, A. Y.; Edinger, P.; Sattari, H.; Gylfason, K. B.; Quack, N. MEMS for Photonic Integrated Circuits. *IEEE J. Sel. Top. Quantum Electron.* **2020**, *26*, 1−16.

(11) Koeber, S.; Palmer, R.; Lauermann, M.; Heni, W.; Elder, D. L.; Korn, D.; Woessner, M.; Alloatti, L.; Koenig, S.; Schindler, P. C.; Yu, H.; Bogaerts, W.; Dalton, L. R.; Freude, W.; Leuthold, J.; Koos, C. Femtojoule Electro-Optic Modulation Using a Silicon−Organic Hybrid Device. *Light: Sci. Appl.* **2015**, *4*, e255−e255.

(12) He, M.; Xu, M.; Ren, Y.; Jian, J.; Ruan, Z.; Xu, Y.; Gao, S.; Sun, S.; Wen, X.; Zhou, L.; Liu, L.; Guo, C.; Chen, H.; Yu, S.; Liu, L.; Cai, X. High-Performance Hybrid Silicon and Lithium Niobate Mach−Zehnder Modulators for 100 Gbit s −1 and Beyond. *Nat. Photonics* **2019**, *13*, 359−364.

(13) Xu, P.; Zheng, J.; Doylend, J. K.; Majumdar, A. Low-Loss and Broadband Nonvolatile Phase-Change Directional Coupler Switches. *ACS Photonics* **2019**, *6*, 553−557.

(14) Wuttig, M.; Bhaskaran, H.; Taubner, T. Phase-Change Materials for Non-Volatile Photonic Applications. *Nat. Photonics* **2017**, *11*, 465−476.

(15) Fang, Z.; Chen, R.; Zheng, J.; Majumdar, A. Non-Volatile Reconfigurable Silicon Photonics Based on Phase-Change Materials. *IEEE J. Sel. Top. Quantum Electron.* **2021**, 1−1.

(16) Abdollahramezani, S.; Hemmatyar, O.; Taghinejad, H.; Krasnok, A.; Kiarashinejad, Y.; Zandehshahvar, M.; Alù, A.; Adibi, A. Tunable Nanophotonics Enabled by Chalcogenide Phase-Change Materials. *Nanophotonics* **2020**, *9*, 1189−1241.

(17) Raoux, S.; Xiong, F.; Wuttig, M.; Pop, E. Phase Change Materials and Phase Change Memory. *MRS Bull.* **2014**, *39*, 703−710.

(18) Shportko, K.; Kremers, S.; Woda, M.; Lencer, D.; Robertson, J.; Wuttig, M. Resonant Bonding in Crystalline Phase-Change Materials. *Nat. Mater.* **2008**, *7*, 653−658.

(19) Pernice, W. H. P.; Bhaskaran, H. Photonic Non-Volatile Memories Using Phase Change Materials. *Appl. Phys. Lett.* **2012**, *101*, 171101.

(20) Ríos, C.; Stegmaier, M.; Hosseini, P.; Wang, D.; Scherer, T.; Wright, C. D.; Bhaskaran, H.; Pernice, W. H. P. Integrated All-Photonic Non-Volatile Multi-Level Memory. *Nat. Photonics* **2015**, *9*, 725−732.

(21) Li, X.; Youngblood, N.; Ríos, C.; Cheng, Z.; Wright, C. D.; Pernice, W. H.; Bhaskaran, H. Fast and Reliable Storage Using a 5 Bit, Nonvolatile Photonic Memory Cell. *Optica* **2019**, *6*, 1−6.

(22) Rios, C.; Hosseini, P.; Wright, C. D.; Bhaskaran, H.; Pernice, W. H. P. On-Chip Photonic Memory Elements Employing Phase-Change Materials. *Adv. Mater.* **2014**, *26*, 1372−1377.
(23) Cheng, Z.; Ríos, C.; Youngblood, N.; Wright, C. D.; Pernice, W. H. P.; Bhaskaran, H. Device-Level Photonic Memories and Logic Applications Using Phase-Change Materials. *Adv. Mater.* **2018**, *30*, No. 1802435.
(24) Feldmann, J.; Youngblood, N.; Karpov, M.; Gehring, H.; Li, X.; Stappers, M.; Le Gallo, M.; Fu, X.; Lukashchuk, A.; Raja, A. S.; Liu, J.; Wright, C. D.; Sebastian, A.; Kippenberg, T. J.; Pernice, W. H. P.; Bhaskaran, H. Parallel Convolutional Processing Using an Integrated Photonic Tensor Core. *Nature* **2021**, *589*, 52−58.
(25) Ríos, C.; Youngblood, N.; Cheng, Z.; Le Gallo, M.; Pernice, W. H. P.; Wright, C. D.; Sebastian, A.; Bhaskaran, H. In-Memory Computing on a Photonic Platform. *Sci. Adv.* **2019**, *5*, No. eaau5759.
(26) Feldmann, J.; Youngblood, N.; Wright, C. D.; Bhaskaran, H.; Pernice, W. H. P. All-Optical Spiking Neurosynaptic Networks with Self-Learning Capabilities. *Nature* **2019**, *569*, 208−214.
(27) Wu, C.; Yu, H.; Lee, S.; Peng, R.; Takeuchi, I.; Li, M. Programmable Phase-Change Metasurfaces on Waveguides for Multimode Photonic Convolutional Neural Network. *Nat. Commun.* **2021**, *12*, 96.
(28) Zheng, J.; Fang, Z.; Wu, C.; Zhu, S.; Xu, P.; Doylend, J. K.; Deshmukh, S.; Pop, E.; Dunham, S.; Li, M.; Majumdar, A. Nonvolatile Electrically Reconfigurable Integrated Photonic Switch Enabled by a Silicon PIN Diode Heater. *Adv. Mater.* **2020**, *32*, No. 2001218.
(29) Zhang, H.; Zhou, L.; Lu, L.; Xu, J.; Wang, N.; Hu, H.; Rahman, B. M. A.; Zhou, Z.; Chen, J. Miniature Multilevel Optical Memristive Switch Using Phase Change Material. *ACS Photonics* **2019**, *6*, 2205−2212.
(30) Ríos, C.; Du, Q.; Zhang, Y.; Popescu, C.-C.; Shalaginov, M. Y.; Miller, P.; Roberts, C.; Kang, M.; Richardson, K. A.; Gu, T.; Vitale, S. A.; Hu, J. Ultra-Compact Nonvolatile Photonics Based on Electrically Reprogrammable Transparent Phase Change Materials. *arXiv:2105.06010 [cond-mat, physics:physics]*, 2021. (Accessed April 25, 2022).
(31) Wang, Y.; Landreman, P.; Schoen, D.; Okabe, K.; Marshall, A.; Celano, U.; Wong, H.-S. P.; Park, J.; Brongersma, M. L. Electrical Tuning of Phase-Change Antennas and Metasurfaces. *Nat. Nanotechnol.* **2021**, *16*, 667−672.
(32) Lepeshov, S.; Krasnok, A. Tunable Phase-Change Metasurfaces. *Nat. Nanotechnol.* **2021**, *16*, 615−616.
(33) Abdollahramezani, S.; Hemmatyar, O.; Taghinejad, M.; Taghinejad, H.; Krasnok, A.; Eftekhar, A. A.; Teichrib, C.; Deshmukh, S.; El-Sayed, M. A.; Pop, E.; Wuttig, M.; Alù, A.; Cai, W.; Adibi, A. Electrically Driven Reprogrammable Phase-Change Metasurface Reaching 80% Efficiency. *Nat. Commun.* **2022**, *13*, 1696.
(34) Kato, K.; Kuwahara, M.; Kawashima, H.; Tsuruoka, T.; Tsuda, H. Current-Driven Phase-Change Optical Gate Switch Using Indium−Tin-Oxide Heater. *Appl. Phys. Express* **2017**, *10*, No. 072201.
(35) Zhang, H.; Zhou, L.; Xu, J.; Wang, N.; Hu, H.; Lu, L.; Rahman, B. M. A.; Chen, J. Nonvolatile Waveguide Transmission Tuning with Electrically-Driven Ultra-Small GST Phase-Change Material. *Sci. Bull.* **2019**, *64*, 782−789.
(36) Taghinejad, H.; Taghinejad, H.; Abdollahramezani, S.; Abdollahramezani, S.; Eftekhar, A. A.; Eftekhar, A. A.; Fan, T.; Hosseinnia, A. H.; Hemmatyar, O.; Dorche, A. E.; Gallmon, A.; Adibi, A. ITO-Based Microheaters for Reversible Multi-Stage Switching of Phase-Change Materials: Towards Miniaturized beyond-Binary Reconfigurable Integrated Photonics. *Opt. Express* **2021**, *29*, 20449−20462.
(37) Zheng, J.; Khanolkar, A.; Xu, P.; Colburn, S.; Deshmukh, S.; Myers, J.; Frantz, J.; Pop, E.; Hendrickson, J.; Doylend, J.; Boechler, N.; Majumdar, A. GST-on-Silicon Hybrid Nanophotonic Integrated Circuits: A Non-Volatile Quasi-Continuously Reprogrammable Platform. *Opt. Mater. Express* **2018**, *8*, 1551−1561.
(38) Wu, C.; Yu, H.; Li, H.; Zhang, X.; Takeuchi, I.; Li, M. Low-Loss Integrated Photonic Switch Using Subwavelength Patterned Phase Change Material. *ACS Photonics* **2019**, *6*, 87−92.
(39) Seok, T. J.; Kwon, K.; Henriksson, J.; Luo, J.; Wu, M. C. Wafer-Scale Silicon Photonic Switches beyond Die Size Limit. *Optica* **2019**, *6*, 490−494.
(40) Zhang, Q.; Zhang, Y.; Li, J.; Soref, R.; Gu, T.; Hu, J. Broadband Nonvolatile Photonic Switching Based on Optical Phase Change Materials: Beyond the Classical Figure-of-Merit. *Opt. Lett.* **2018**, *43*, 94−97.
(41) De Leonardis, F.; Soref, R.; Passaro, V. M. N.; Zhang, Y.; Hu, J. Broadband Electro-Optical Crossbar Switches Using Low-Loss $Ge_2Sb_2Se_4Te_1$ Phase Change Material. *J. Lightwave Technol.* **2019**, *37*, 3183−3191.
(42) Zhang, Y.; Zhang, Q.; Ríos, C.; Shalaginov, M. Y.; Chou, J. B.; Roberts, C.; Miller, P.; Robinson, P.; Liberman, V.; Kang, M.; Richardson, K. A.; Gu, T.; Vitale, S. A.; Hu, J. Transient Tap Couplers for Wafer-Level Photonic Testing Based on Optical Phase Change Materials. *ACS Photonics* **2021**, *8*, 1903−1908.
(43) Zheng, J.; Zhu, S.; Xu, P.; Dunham, S.; Majumdar, A. Modeling Electrical Switching of Nonvolatile Phase-Change Integrated Nanophotonic Structures with Graphene Heaters. *ACS Appl. Mater. Interfaces* **2020**, *12*, 21827−21836.
(44) Du, P.-Y.; Wu, J.-Y.; Hsu, T.-H.; Lee, M.-H.; Wang, T.-Y.; Cheng, H.-Y.; Lai, E.-K.; Lai, S.-C.; Lung, H.-L.; Kim, S.; BrightSky, M. J.; Zhu, Y.; Mittal, S.; Cheek, R.; Raoux, S.; Joseph, E. A.; Schrott, A.; Li, J.; Lam, C. The Impact of Melting during Reset Operation on the Reliability of Phase Change Memory. In *2012 IEEE International Reliability Physics Symposium (IRPS)*, 2012; pp 6C.2.1-6C.2.6.
(45) Delaney, M.; Zeimpekis, I.; Du, H.; Yan, X.; Banakar, M.; Thomson, D. J.; Hewak, D. W.; Muskens, O. L. Nonvolatile Programmable Silicon Photonics Using an Ultralow-Loss Sb2Se3 Phase Change Material. *Sci. Adv.* **2021**, *7*, No. eabg3500.
(46) Stegmaier, M.; Ríos, C.; Bhaskaran, H.; Wright, C. D.; Pernice, W. H. P. Nonvolatile All-Optical 1 × 2 Switch for Chipscale Photonic Networks. *Adv. Opt. Mater.* **2017**, *5*, No. 1600346.
(47) Delaney, M.; Zeimpekis, I.; Lawson, D.; Hewak, D. W.; Muskens, O. L. A New Family of Ultralow Loss Reversible Phase-Change Materials for Photonic Integrated Circuits: Sb2S3 and Sb2Se3. *Adv. Funct. Mater.* **2020**, *30*, No. 2002447.
(48) Dong, W.; Liu, H.; Behera, J. K.; Lu, L.; Ng, R. J. H.; Sreekanth, K. V.; Zhou, X.; Yang, J. K. W.; Simpson, R. E. Wide Bandgap Phase Change Material Tuned Visible Photonics. *Adv. Funct. Mater.* **2019**, *29*, No. 1806181.
(49) Fang, Z.; Zheng, J.; Saxena, A.; Whitehead, J.; Chen, Y.; Majumdar, A. Non-Volatile Reconfigurable Integrated Photonics Enabled by Broadband Low-Loss Phase Change Material. *Adv. Opt. Mater.* **2021**, *9*, No. 2002049.
(50) Zhang, Y.; Chou, J. B.; Li, J.; Li, H.; Du, Q.; Yadav, A.; Zhou, S.; Shalaginov, M. Y.; Fang, Z.; Zhong, H.; Roberts, C.; Robinson, P.; Bohlin, B.; Ríos, C.; Lin, H.; Kang, M.; Gu, T.; Warner, J.; Liberman, V.; Richardson, K.; Hu, J. Broadband Transparent Optical Phase Change Materials for High-Performance Nonvolatile Photonics. *Nat. Commun.* **2019**, *10*, 4279.
(51) Kim, S.; Burr, G. W.; Kim, W.; Nam, S.-W. Phase-Change Memory Cycling Endurance. *MRS Bull.* **2019**, *44*, 710−714.
(52) Meng, J.; Peserico, N.; Ma, X.; Zhang, Y.; Popescu, C.-C.; Kang, M.; Miscuglio, M.; Richardson, K.; Hu, J.; Sorger, V. J. Electrical Programmable Low-Loss High Cyclable Nonvolatile Photonic Random-Access Memory, 2022. (Accessed April 25, 2022).
(53) Watts, M. R.; Sun, J.; DeRose, C.; Trotter, D. C.; Young, R. W.; Nielson, G. N. Adiabatic Thermo-Optic Mach−Zehnder Switch. *Opt. Lett.* **2013**, *38*, 733.
(54) Kieninger, C.; Kieninger, C.; Kieninger, C.; Kutuvantavida, Y.; Kutuvantavida, Y.; Elder, D. L.; Wolf, S.; Zwickel, H.; Blaicher, M.; Kemal, J. N.; Lauermann, M.; Randel, S.; Freude, W.; Dalton, L. R.; Koos, C.; Koos, C. Ultra-High Electro-Optic Activity Demonstrated in a Silicon-Organic Hybrid Modulator. *Optica* **2018**, *5*, 739−748.

https://doi.org/10.1021/acsphotonics.2c00452
ACS Photonics XXXX, XXX, XXX−XXX

(55) Qiu, C.; Gao, W.; Soref, R.; Robinson, J. T.; Xu, Q. Reconfigurable Electro-Optical Directed-Logic Circuit Using Carrier-Depletion Micro-Ring Resonators. *Opt. Lett.* **2014**, *39*, 6767−6770.
(56) Haffner, C.; Joerg, A.; Doderer, M.; Mayor, F.; Chelladurai, D.; Fedoryshyn, Y.; Roman, C. I.; Mazur, M.; Burla, M.; Lezec, H. J.; Aksyuk, V. A.; Leuthold, J. Nano−Opto-Electro-Mechanical Switches Operated at CMOS-Level Voltages. *Science* **2019**, *366*, 860−864.

https://doi.org/10.1021/acsphotonics.2c00452
ACS Photonics XXXX, XXX, XXX−XXX